

# High-temperature ferrimagnetic order triggered metal-to-insulator transition in $\text{CaCu}_3\text{Ni}_2\text{Os}_2\text{O}_{12}$

Received: 14 May 2024

Accepted: 8 April 2025

Published online: 21 April 2025

 Check for updates

Xubin Ye<sup>1,9</sup>, Yunyu Yin<sup>1,2,9</sup>, Yingying Cao<sup>1,2</sup>, Zhiyu Liao<sup>1</sup>, Xiao Wang<sup>1,2</sup>, Min Liu<sup>1</sup>, Qianqian Wang<sup>1,2</sup>, Zhao Pan<sup>1,2</sup>, Zhiwei Hu<sup>3</sup>, Hong-Ji Lin<sup>4</sup>, Chien Te Chen<sup>4</sup>, Chih-Wen Pao<sup>4</sup>, Philippe Ohresser<sup>5</sup>, Lucie Nataf<sup>5</sup>, François Baudelet<sup>5</sup>, Wenyun Yang<sup>6</sup>, Jinbo Yang<sup>6</sup>, Jinguang Cheng<sup>1,2,7</sup>, Pu Yu<sup>8</sup>, Xianggang Qiu<sup>1,2,7</sup>, Yi-feng Yang<sup>1,2,7</sup> ✉, Tao Xiang<sup>1,2,7</sup> & Youwen Long<sup>1,2,7</sup> ✉

Ferromagnetic order-induced insulator-to-metal transitions via the double exchange mechanism have been studied widely. In contrast, ferromagnetic or ferrimagnetic spontaneous magnetization induced metal-to-insulator transitions (MITs), especially occurring above room temperature, remain extremely limited, although such magnetoelectric materials hold great potential for low-loss multifunctional electronic and spintronic devices. Here, a novel  $3d/5d$  hybridized quadruple perovskite oxide,  $\text{CaCu}_3\text{Ni}_2\text{Os}_2\text{O}_{12}$ , was synthesized. It undergoes long-range  $\text{Cu}^{2+}(\uparrow)\text{-Ni}^{2+}(\uparrow)\text{-Os}^{6+}(\downarrow)$  ferrimagnetic order with a high Curie temperature of 393 K, maintaining a saturated magnetization of  $2.15 \mu_B/\text{f.u.}$  at 300 K. Intriguingly, an MIT is found to occur concurrently at the Curie temperature. Theoretical analyses reveal that the ferrimagnetic spontaneous order significantly renormalizes the electronic band structure, which can be further modified by electronic correlation and spin-orbit coupling effects, leading to the MIT via the Lifshitz-type mechanism. This work thus provides a paradigm material to realize ferrimagnetic spontaneous magnetization induced MIT at a high critical temperature toward advanced applications.

The metal-insulator transition has been an enduring central topic in condensed matter physics<sup>1</sup>. For example, ferromagnetic (FM) order induced electrical transitions from insulator to metal have received much attention in manganese oxides based on the double exchange mechanism<sup>2-5</sup>. In contrast, however, the materials which show FM or ferrimagnetic (FiM) spontaneous magnetization triggered metal-to-insulator transitions (MITs), especially with high Curie temperatures

(above room temperature), are little known. Considering that the FM/FiM and insulating states favor transport of spin instead of charge, such materials provide promising applications for low-dissipation electronic and spintronic devices, bifunctional thermal sensors, integrated computing and storage systems etc<sup>6-8</sup>.

Mott first proposed that strong intra-atomic electron-electron Coulomb repulsion ( $U$ ) can open an energy gap near the Fermi level,

<sup>1</sup>Beijing National Laboratory for Condensed Matter Physics, Institute of Physics, Chinese Academy of Sciences, Beijing, China. <sup>2</sup>University of Chinese Academy of Sciences, Beijing, China. <sup>3</sup>Max Planck Institute for Chemical Physics of Solids, Dresden, Germany. <sup>4</sup>National Synchrotron Radiation Research Center, Hsinchu, Taiwan. <sup>5</sup>Synchrotron SOLEIL, L'Orme des Merisiers, Gif-sur-Yvette, France. <sup>6</sup>State Key Laboratory for Mesoscopic Physics, School of Physics, Peking University, Beijing, China. <sup>7</sup>Songshan Lake Materials Laboratory, Dongguan, China. <sup>8</sup>State Key Laboratory of Low Dimensional Quantum Physics and Department of Physics, Tsinghua University, Beijing, China. <sup>9</sup>These authors contributed equally: Xubin Ye, Yunyu Yin. ✉ e-mail: [yifeng@iphy.ac.cn](mailto:yifeng@iphy.ac.cn); [ywlong@iphy.ac.cn](mailto:ywlong@iphy.ac.cn)

facilitating an MIT as  $U$  is enhanced to a moderate value at a critical temperature ( $T_{\text{MI}}$ )<sup>9,10</sup>. In addition, electronic interactions across atoms in the spin space may change the band structures of substances. In 1951<sup>11</sup>, Slater elaborated that, in a half-filled  $d$ -electron system, the alternating arrangement of spins in opposite directions can double the atomic periodicity, split each band in half, and form an energy gap when a spin order occurs. Thus, a collinear antiferromagnetic (AFM) order may also drive the MIT, as observed in  $\text{NaOsO}_3$ <sup>12</sup>. In principle, however, spontaneous magnetization is not expected to occur in the Mott and Slater mechanisms. How to realize FM or FiM spontaneous magnetization induced MIT has been subjected to a challenge at present. Beyond Mott and Slater's regimes, the Lifshitz transition can open a band gap due to changes in the Fermi surface topology, driven by internal or external parameters such as chemical doping or pressure. The spin-driven Lifshitz transition, which may occur in materials with weaker electron-electron correlation, dispersed energy bands, small local spins, and strong orbital hybridization, provides an opportunity to realize spontaneous magnetization triggered MIT. Such materials reside at the threshold of magnetic and electrical instability. As a result, the variations in spin amplitude and direction may continuously reduce the electron or hole pockets at the Fermi surface, which is a defining characteristic of the Lifshitz-type process<sup>13–15</sup>, ultimately leading to an MIT. This mechanism is particularly pertinent in  $3d$ – $5d$  hybridized systems, since a delicate balance among band

hybridization, electronic correlation, and spin–orbital coupling (SOC) plays a crucial role for magnetic and electrical properties.

Both A- and B-site ordered quadruple perovskite oxide with chemical formula  $\text{AA}_3\text{B}_2\text{B}'_2\text{O}_{12}$ , as shown in Fig. 1a, can accommodate magnetic transition metals at three different atomic positions (A', B, and B' sites). Such a peculiar structure provides a new avenue for investigating multiband-induced MIT integrating with FM or FiM spin configurations. In this work, a novel quadruple perovskite oxide,  $\text{CaCu}_3\text{Ni}_2\text{Os}_2\text{O}_{12}$  (CCNOO), was prepared at 8 GPa and 1423 K. The strong  $3d$ – $5d$  hybridized effects via Cu–O–Os pathways cause metallic electrical behavior at higher temperatures. However, the long-range Cu( $\uparrow$ )–Ni( $\uparrow$ )–Os( $\downarrow$ ) FiM order with robust spontaneous magnetization triggers a MIT via the Lifshitz's regime at the onset temperature of  $T_{\text{MI}} = T_{\text{C}} = 393$  K. Thus, the current CCNOO provides a rare material system which shows FiM spontaneous magnetization induced MIT above room temperature with potential applications for advanced electronic and spintronic devices.

## Results

### Crystal structure of CCNOO

Figure 1b illustrates the synchrotron powder X-ray diffraction (SXRD) pattern and related Rietveld refinement results for CCNOO at 300 K. A more detailed view for the low-angle region, with a reduced intensity scale, is provided in Supplementary Fig. S1. All diffraction peaks, except for a minor impurity peak from  $\text{OsO}_2$  (see Fig. S1), can be indexed to a cubic Bravais lattice. Detailed Rietveld analysis confirms that the compound crystallizes into a both A- and B-site ordered quadruple perovskite structure with the space group  $Pn-3$  (no. 201) and lattice constant  $a = 7.40776(1)$  Å. The sharp diffraction peaks with the Miller indices  $h + k + l = \text{odd}$ , such as (111) and (311) (highlighted in red in Fig. 1b), strongly indicate the rock-salt-type ordering of Ni and Os at the B-site. As seen from the crystal structure (Fig. 1a), in CCNOO, the alternately distributed B-site  $\text{NiO}_6$  and B'-site  $\text{OsO}_6$  octahedra connect by sharing corner O atoms. The A'-site  $\text{CuO}_4$  squares are also linked to Ni/OsO<sub>6</sub> octahedra via corner-sharing O atoms. Compared to double perovskites  $\text{A}_2\text{NiOsO}_6$  ( $\text{A} = \text{Ca}, \text{Sr}, \text{and Ba}$ ), significant changes in the local coordination environment at the A' site in CCNOO lead to sharp tilting of the Ni/OsO<sub>6</sub> octahedra with a heavily reduced Ni–O–Os bond angle to  $138.5^\circ$ <sup>16–18</sup>. Moreover, peculiar Cu–O–Ni/Os pathways exist with the bond angle of about  $110^\circ$  in CCNOO. These features significantly enhance the orbital overlap and hybridization between  $3d$   $\text{Cu}^{2+}/\text{Ni}^{2+}$  and  $5d$   $\text{Os}^{6+}$  ions via O<sup>2–</sup>. Benefiting from the strong X-ray scattering contrast between  $3d$ -Ni and  $5d$ -Os, the refined occupancy factor (99.7%) reveals a nearly fully ordered distribution for these two atoms, as observed previously in  $\text{A}_2\text{NiOsO}_6$ . The refined structural parameters are listed in Supplementary Tables S1 and S2. According to the bond lengths, bond valence sum calculations indicate that the charge combination is  $\text{CaCu}^{2+}_3\text{Ni}^{2+}_2\text{Os}^{6+}_2\text{O}_{12}$ , in good agreement with the element-selective X-ray absorption spectroscopy (XAS) results<sup>20–22</sup>. As shown in Supplementary Fig. S2, all the Cu-, Ni- $L_{2,3}$ , and Os- $L_3$  XAS spectra exhibit very similar spectral features, such as peak energy positions and spectral shapes, with those of standard  $\text{CaCu}^{2+}_3\text{Ti}_4\text{O}_{12}$ ,  $\text{Ni}^{2+}\text{O}$ , and  $\text{Ba}_2\text{NiOs}^{6+}\text{O}_6$  references, respectively, revealing the formation of  $\text{Cu}^{2+}$ ,  $\text{Ni}^{2+}$ , and  $\text{Os}^{6+}$  in CCNOO.

### Magnetic properties and spin structure of CCNOO

Figure 2a depicts the temperature dependence of the magnetic susceptibility ( $\chi$ ) of CCNOO. As the temperature decreases to a critical value of  $T_{\text{C}} = 393$  K,  $\chi$  experiences a sharp increase, suggesting the occurrence of an FM-like phase transition. Above  $T_{\text{C}}$  (400–500 K), the paramagnetic (PM)  $\chi^1(T)$  data deviate from the linear Curie–Weiss (CW) law, whereas it can be well fitted by the Néel FiM theory with the function  $\chi^1 = (T - \theta)/C - \zeta/(T - \theta)^{2.3}$ , where the first term symbolizes the CW behavior in the high-temperature limit, and the second represents hyperbolic behavior near the FiM order. The fitted FiM Curie

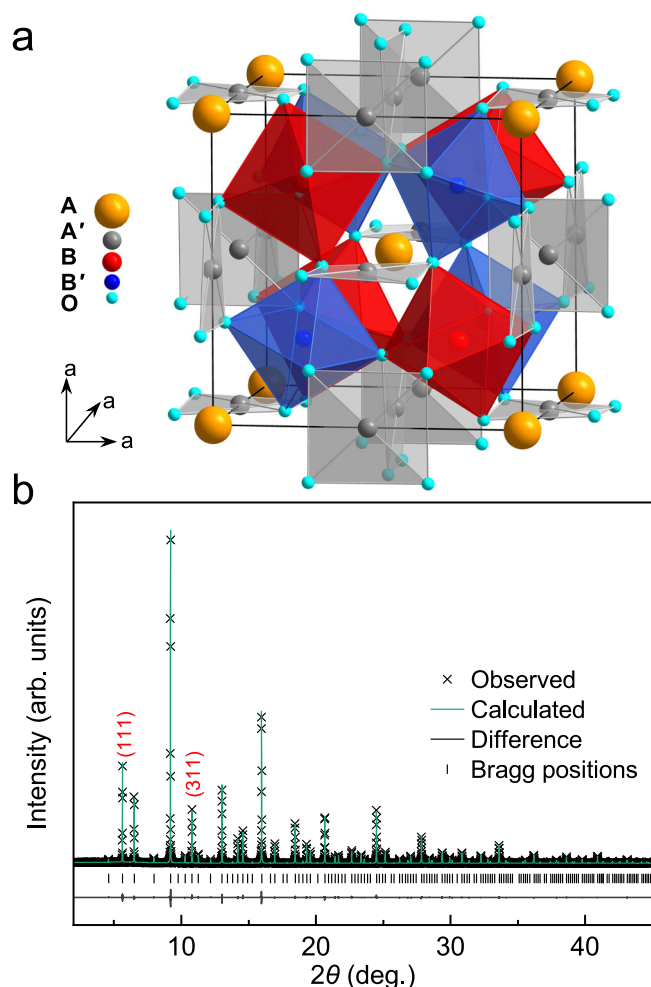


**Fig. 1 | Synthesis and crystal structure of CCNOO.** **a** Schematic crystal structure of both A- and B-site ordered quadruple perovskite oxide  $\text{AA}_3\text{B}_2\text{B}'_2\text{O}_{12}$ . The corner-sharing B/B'O<sub>6</sub> octahedra and A'O<sub>4</sub> planar squares are shown. **b** SXRD pattern and Rietveld refinement results for CCNOO at room temperature. The black ticks indicate the allowed Bragg reflections with space group  $Pn-3$ .

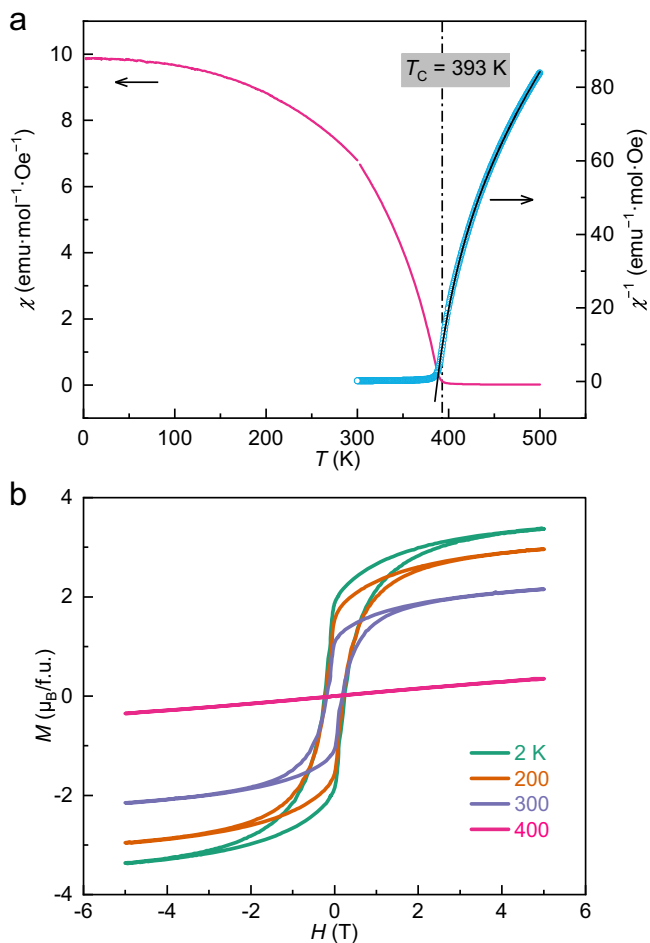


**Fig. 2 | Magnetic properties of CCNOO.** Temperature dependence of (a) magnetic susceptibility  $\chi$  and its inverse measured at 0.1 T, b the isothermal magnetization loops measured at different temperatures. The black curve in (a) shows the Néel FiM model fitting for  $\chi^{-1}$  above 400 K.

temperature is 389 K, agreeing well with  $T_C$ . In the high-temperature limit, the effective magnetic moment is fitted to be  $5.20 \mu_B/f.u.$  This value is comparable to the theoretical one ( $5.51 \mu_B/f.u.$ ) obtained by considering the spin-only contribution of  $Cu^{2+}$  and  $Ni^{2+}$ , as well as the SOC effect of  $Os^{6+}$ . Therefore, the long-range FiM transition can be assigned to CCNOO at  $T_C = 393$  K. Figure 2b shows the isothermal magnetization curves. Below  $T_C$ , canonical magnetic hysteresis loops with coercive fields of about 0.24 T are observed. The saturated moment observed at 300 K and 5 T is  $2.15 \mu_B/f.u.$ , which further increases to  $3.36 \mu_B/f.u.$  at 2 K, in coherence with X-ray magnetic circular dichroism (XMCD) results shown below.

Because there are three different kinds of magnetic ions ( $Cu^{2+}$ ,  $Ni^{2+}$ , and  $Os^{6+}$ ) in CCNOO, element-selective XMCD is a desirable method not only for determining the magnetic configuration but also for obtaining the spin moment ( $m_s$ ) and orbital moment ( $m_l$ ) of each element<sup>24–26</sup>. Figure 3a–c presents the spectra at the Cu-, Ni-, and Os- $L_{2,3}$  edges, respectively. The Cu- and Ni- $L_3$  XMCD results exhibit negative signals, while the Cu- and Ni- $L_2$  signals are positive; inverse signs are observed at the Os- $L_{2,3}$  edges. These features indicate that the spins of  $Cu^{2+}$  and  $Ni^{2+}$  align parallel to each other but antiparallel to that of  $Os^{6+}$ , demonstrating the formation of a  $Cu^{2+}(\uparrow)-Ni^{2+}(\uparrow)-Os^{6+}(\downarrow)$  FiM order (refer to Fig. 3f), as expected from the Néel FiM theory. By utilizing the sum rules<sup>27,28</sup>, one can further acquire the  $m_s$  and  $m_l$  of  $Cu^{2+}$ ,  $Ni^{2+}$ , and  $Os^{6+}$ . As summarized in Supplementary Table S3, the derived  $m_{tot}$  values for  $Cu^{2+}$ ,  $Ni^{2+}$ , and  $Os^{6+}$  are 0.31, 1.43, and  $-0.21 \mu_B$ , respectively, yielding  $m_{tot} = 3.37 \mu_B/f.u.$  for CCNOO. This value agrees

well with the magnetization measured at 2 K. The reduced spin moments, below single-ion theoretical values, for these magnetic cations most probably arise from strong orbital hybridization within the  $Cu^{2+}-Ni^{2+}-Os^{6+}$  covalent framework via oxygen, as indicated by theoretical calculations (shown later). Moreover, the  $m_l/m_s$  ratios of  $Cu^{2+}$ ,  $Ni^{2+}$ , and  $Os^{6+}$  were calculated to be 0.22, 0.28, and 0.22, respectively. Thus, significant orbital moments are present for 3d  $Cu^{2+}$  and  $Ni^{2+}$  in CCNOO, in addition to 5d  $Os^{6+}$ . The large  $m_l/m_s$  ratio for  $Ni^{2+}$  may be primarily attributed to the  $t_{2g}^5 e_g^3$  state, as reported for  $NiO$ <sup>29</sup> and  $NiFe_2O_4$ <sup>30</sup>, whereas the considerable orbital moment of  $Cu^{2+}$  is a result of the strong hybridization effect between 3d  $Cu^{2+}$  and 5d  $Os^{6+}$ , as will be discussed later. The FiM order of CCNOO was further supported by neutron powder diffraction (NPD) experiments from 3.5 K to 400 K, as shown in Fig. 3d and Supplementary Fig. S3. The magnetic diffraction can be interpreted based on a collinear  $Cu^{2+}(\uparrow)-Ni^{2+}(\uparrow)-Os^{6+}(\downarrow)$  FiM order with the wave vector  $k = (0, 0, 0)$ , in accordance with the XMCD results. Due to the intrinsic resolution limitation of the NPD technique, particularly the weak magnetic scattering contribution, direct determination of the magnitudes and orientations of  $Cu^{2+}$  and  $Os^{6+}$  magnetic moments is not accurately achievable. Consequently, we are only able to refine the  $Ni^{2+}$  magnetic moment as a function of temperature as depicted in Fig. 3e. One finds that the relationship conforms to the Brillouin function, with the magnetic moment nearly reaching saturation at 200 K. Note that, within the current NPD resolution, one cannot determine whether there is a small amount of non-collinear spin component potentially arising from the SOC effect.

### Electrical transport properties of CCNOO

The resistivity as a function of temperature is presented in Fig. 4a for CCNOO. Above  $T_C$  (393–550 K), the resistivity remains nearly constant, exhibiting minimal temperature dependence and maintaining a low value of approximately  $4 \times 10^{-4} \Omega \cdot cm$ . This behavior may imply metallic electrical transport property, if one considers the grain boundary effects and possible impurity scattering due to the polycrystalline nature of the sample. As the temperature decreased to  $T_{MI} = T_C = 393$  K, the resistivity began to sharply increase, with a large negative derivative ( $d\rho/dT < 0$ ), indicating the presence of an insulating/semiconducting feature. This result suggests that an MIT-like transition takes place at the onset temperature of the FiM phase transition. This transition can also be confirmed by the calorimetric measurement. As shown in Supplementary Fig. S4, both heating and cooling differential scanning calorimetry curves display a step-like anomaly around  $T_{MI}$  ( $T_C$ ) without any heat hysteresis, suggesting the second-order nature of the transition. The  $\rho(T)$  data below 110 K can be well described by the 3D Mott's variable-range-hopping (VRH) model for localized charge carriers, represented by the function  $\rho(T) = \rho_0 \times \exp(T_0/T)^{1/431}$ , where  $\rho_0$  and  $T_0$  are constants. To further illustrate this behavior, the  $\log \rho - T^{-1/4}$  relationship was plotted in Fig. 4b, showing a good linear feature below 110 K and suggesting an insulating ground state of CCNOO. However, between 110 K and 393 K, none of the existing insulating or semiconducting electrical models can reproduce the resistivity data.

The chemical composition of CCNOO is thermally stable at temperatures up to 950 K, as revealed by thermogravimetric measurement (Supplementary Fig. S5). To check whether a structural phase transition occurs or not during the joint FiM and metal-to-insulator transitions, temperature-dependent laboratory XRD was performed. As the temperature varies from 300 to 500 K across  $T_C$  ( $T_{MI}$ ), all the XRD peaks smoothly shift towards lower angles (see Supplementary Fig. S6), as expected from thermal expansion, and there is no trace of structural transformation. Consequently, the cell volume displays a linear relationship with temperature, ruling out structural variation as the origin of the FiM order, as well as the joint MIT occurring at  $T_C$  ( $T_{MI}$ ).

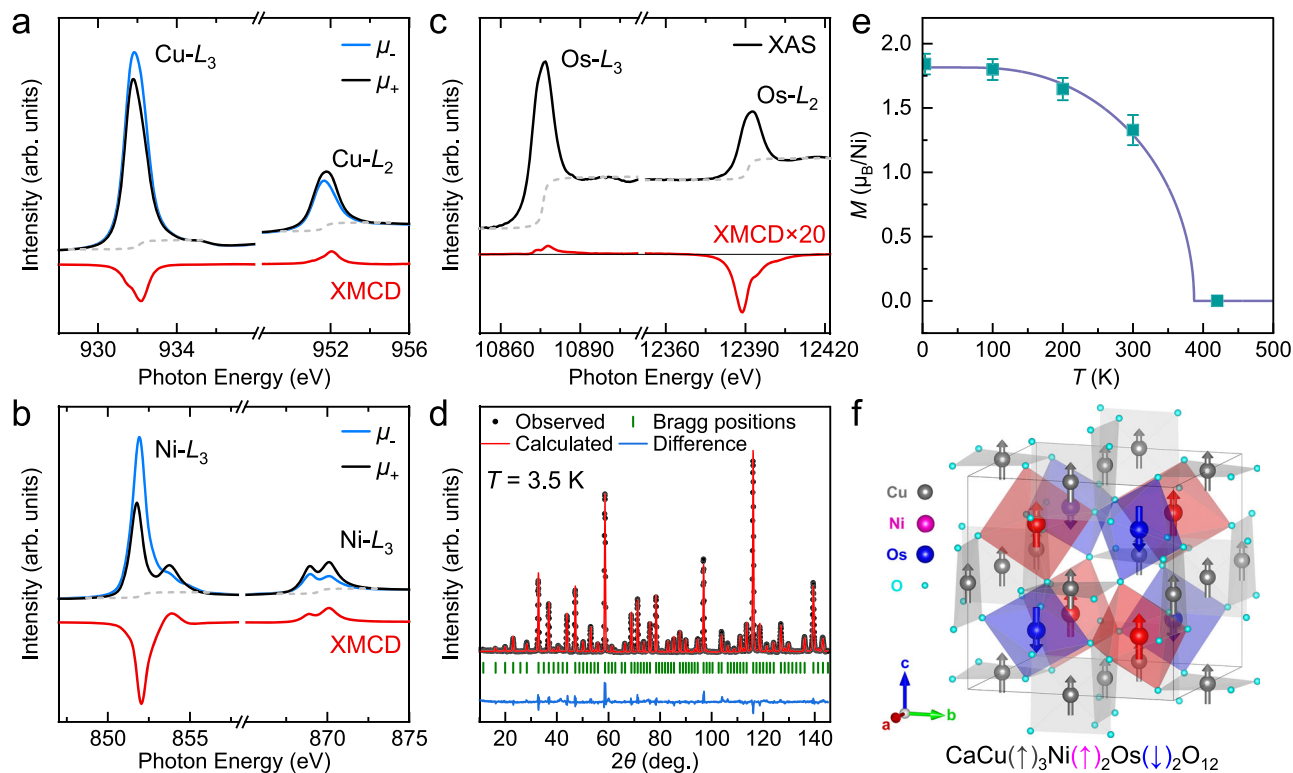


**Fig. 3 | FIM structure in CCNOO.** XMCD of CCNOO near **a** Cu  $L_{2,3}$ , **b** Ni  $L_{2,3}$ , and **c** Os  $L_{2,3}$  edges measured at 10 K. **d** NPD pattern and corresponding Rietveld refinement results of CCNOO at 3.5 K. **e** Temperature dependence of Ni magnetic

moments, with the solid line showing the Brillouin function fitting result. **f** Schematic  $\text{Cu}^{2+}(\uparrow)\text{Ni}^{2+}(\uparrow)\text{Os}^{6+}(\downarrow)$  FiM spin structure.

### Temperature-dependent infrared spectral analysis

Temperature-dependent infrared optical spectroscopy provides deep insights into the evolution of the electrical properties of CCNOO. For a direct absorption edge, the absorption coefficient  $\alpha$  is proportional to  $m_r^{3/2} \sqrt{\hbar\omega - 2\Delta_D}$ , where  $m_r$  and  $2\Delta_D$  represent the effective mass of the electron or hole at band edges and the optical direct gap, respectively. As shown in Fig. 5a, the linear relationship between  $\alpha^2$  and photon energy in a wide energy region illustrates the direct electronic transition in CCNOO. The spectra collected at 390–420 K are nearly completely overlapped, while those below 390 K remarkably shift toward higher energies with decreasing temperature. These features suggest that a bandgap starts to open near  $T_{\text{MI}} (T_C)$  and the magnitude of the gap gradually increases on cooling. Based on the linear fitting and extrapolation to  $\alpha^2 = 0$ , the detailed values of the optical bandgap were obtained. As shown in Fig. 5b, above  $T_{\text{MI}}$ , a small temperature-independent residual optical bandgap is observed due to the polycrystalline nature of the sample. Below  $T_{\text{MI}}$ , however, the optical gap rapidly increases with decreasing temperature, revealing the continuously enhanced band gap. Moreover, the temperature dependence of optical bandgap ( $2\Delta_D$ ) can be well fitted using the Bardeen–Cooper–Schrieffer function<sup>32,33</sup>,  $\frac{E_g(T)}{E_g(0)} = \tanh \frac{E_g(T)T_{\text{tra}}}{E_g(0)T}$ , yielding  $T_{\text{tra}} = 402(1)$  K and  $E_g(0) = 0.193(1)$  eV. The fitted transition temperature ( $T_{\text{tra}}$ ) is comparable to  $T_C (T_{\text{MI}})$ , and the fitted bandgap at 0 K [ $E_g(0)$ ] is similar to that by theoretical calculations (will be shown later). Note that although the infrared spectra start to shift below  $T_{\text{MI}}$ , the slopes for all spectra at different temperatures remain nearly unchanged. This feature suggests the continuous reduction of electron or hole pockets near the Fermi surface, consistent with the Lifshitz-type phase transition mechanism.

### Physical mechanisms of the MIT in CCNOO

The metallic electrical transport of CCNOO above  $T_C (T_{\text{MI}})$  is in sharp contrast to the insulating behavior observed in double perovskites

$\text{A}_2\text{NiOsO}_6$ <sup>16–18</sup>. Considering the similar  $\text{Ni}^{2+}/\text{Os}^{6+}$  charge order in these compounds at the B-site, the introduction of A'-site  $\text{Cu}^{2+}$  in CCNOO should play a crucial role for the essentially different electrical properties. As mentioned in the structural analysis, Cu and Os connect via O, forming Cu–O–Os pathways with a bond angle approaching  $112.4^\circ$ . As a result, strong  $3d-2p-5d$  hybridizations are expected to occur in CCNOO, as illustrated by the large orbital moment of  $\text{Cu}^{2+}$ . Similarly, in another  $3d-5d$  quadruple perovskite metallic oxide  $\text{CaCu}_3\text{Ir}_4\text{O}_{12}$ , considerable Cu–O–Ir hybridized effects were found to occur<sup>19,34</sup>. Therefore, the itinerant  $3d$  electrons of the A'-site  $\text{Cu}^{2+}$  and  $5d$  electrons of the B'-site  $\text{Os}^{6+}$  govern the metallic electrical transport of CCNOO above  $T_C$ . Once the long-range  $\text{Cu}^{2+}(\uparrow)\text{Ni}^{2+}(\uparrow)\text{Os}^{6+}(\downarrow)$  FiM order is formed, the electronic band structures are renormalized, and the bands of  $\text{Cu}^{2+}$  and  $\text{Os}^{6+}$  can be removed from the Fermi surface, causing a significant increase in resistivity below  $T_{\text{MI}} (T_C)$ .

First-principles theoretical calculations based on the generalized gradient approximation (GGA) were conducted to gain further understanding of the magnetic and electrical properties of CCNOO. Four different types of spin structures, including FiM  $\text{Cu}^{2+}(\uparrow)\text{Ni}^{2+}(\uparrow)\text{Os}^{6+}(\downarrow)$ ,  $\text{Cu}^{2+}(\downarrow)\text{Ni}^{2+}(\uparrow)\text{Os}^{6+}(\uparrow)$ ,  $\text{Cu}^{2+}(\downarrow)\text{Ni}^{2+}(\uparrow)\text{Os}^{6+}(\downarrow)$ , and FM  $\text{Cu}^{2+}(\uparrow)\text{Ni}^{2+}(\uparrow)\text{Os}^{6+}(\uparrow)$ , were compared to confirm the magnetic ground state. As shown in Supplementary Fig. S7 and Table S4, our calculations provide a stable  $\text{Cu}^{2+}(\uparrow)\text{Ni}^{2+}(\uparrow)\text{Os}^{6+}(\downarrow)$  ground state, which has much lower free energy than other configurations. Moreover, inside the muffin-tin spheres, the calculated moments are  $0.55 \mu_B$  for  $\text{Cu}^{2+}$ ,  $1.65 \mu_B$  for  $\text{Ni}^{2+}$ , and  $-0.87 \mu_B$  for  $\text{Os}^{6+}$ , leading to a total moment of  $3.21 \mu_B/\text{f.u.}$  The calculated magnetic ground state and moments agree well with experimental results. To further understand the origin of  $\text{Cu}^{2+}(\uparrow)\text{Ni}^{2+}(\uparrow)\text{Os}^{6+}(\downarrow)$  spin coupling, the nearest spin exchange interactions between Cu, Ni, and Os were calculated (refer to Supplementary Fig. S8), yielding  $J_{\text{Cu-Ni}} = -3$  meV,  $J_{\text{Cu-Os}} = 67$  meV, and  $J_{\text{Ni-Os}} = 13$  meV. The AFM  $J_{\text{Cu-Os}}$  and  $J_{\text{Ni-Os}}$ , and FM  $J_{\text{Cu-Ni}}$  interactions are consistent with the FiM  $\text{Cu}^{2+}(\uparrow)\text{Ni}^{2+}(\uparrow)\text{Os}^{6+}(\downarrow)$  spin structure determined in

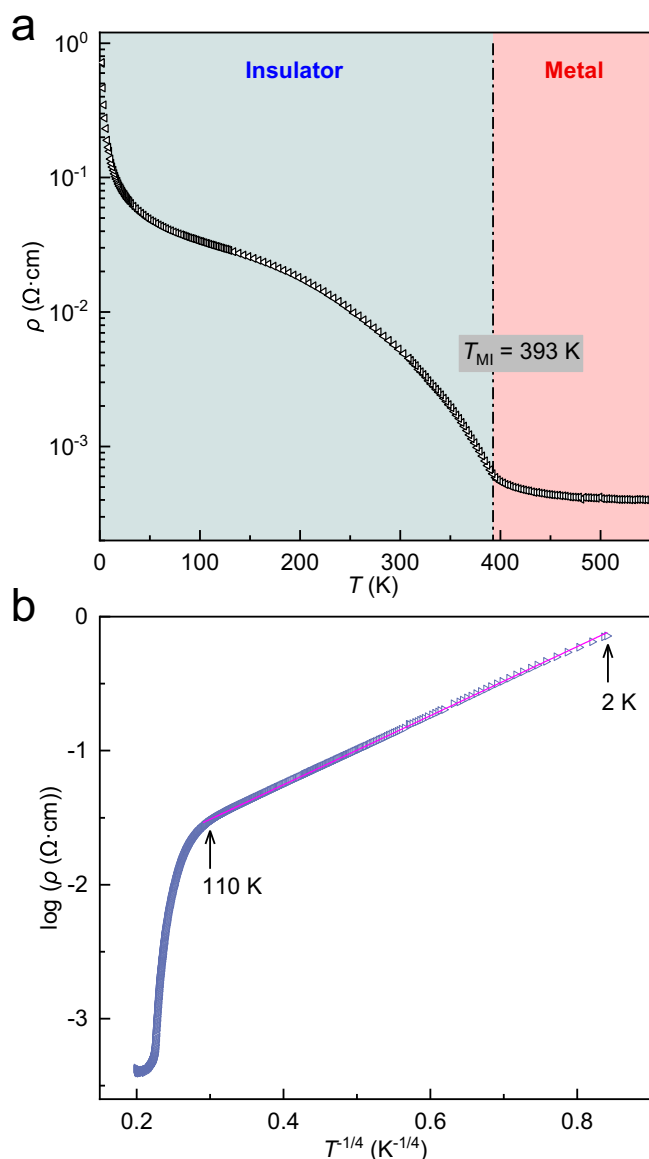


**Fig. 4 | Electrical transport properties of CCNOO.** Temperature dependence of **a** a resistivity  $\rho$ , and **b**  $\log \rho - T^{-1/4}$  plot measured at zero magnetic field for CCNOO. The solid line presents the Mott's 3D VRH model fitting. The vertical dot line indicates the phase transition temperature.

experiments. Note that the intensity of the Cu–Os interaction is much larger than that of the Cu–Ni and Ni–Os interactions, revealing that the strongly hybridized  $\text{Cu}^{2+}$ –O– $\text{Os}^{6+}$  pathways<sup>19,34</sup> dominate the magnetism and electrical transport properties of CCNOO.

The electronic band structure of CCNOO was also determined by theoretical calculations. For comparison, both nonmagnetic (NM) and FiM  $\text{Cu}^{2+}(\uparrow)$ – $\text{Ni}^{2+}(\uparrow)$ – $\text{Os}^{6+}(\downarrow)$  states were used for the calculations. As shown in Fig. 6 and Supplementary Fig. S9, for the NM calculations, the electronic density of states (DOS) always exhibits metallic behavior and considerable Cu–O–Os hybridization regardless of  $U$  and SOC, in agreement with the resistivity data above  $T_C$ . In contrast, once the  $\text{Cu}^{2+}(\uparrow)$ – $\text{Ni}^{2+}(\uparrow)$ – $\text{Os}^{6+}(\downarrow)$  FiM ground state is considered, the band structures near the Fermi surface change significantly (refer to Supplementary Fig. S10). Specifically, a finite pseudogap<sup>14</sup> is found to occur for the FiM GGA calculations, where only a band-crossing point from the Os  $5d$  band induces a slight DOS around the  $R$  point. Therefore, the spin order can significantly renormalize the band structure and considerably deplete the DOS near the Fermi level. When the SOC

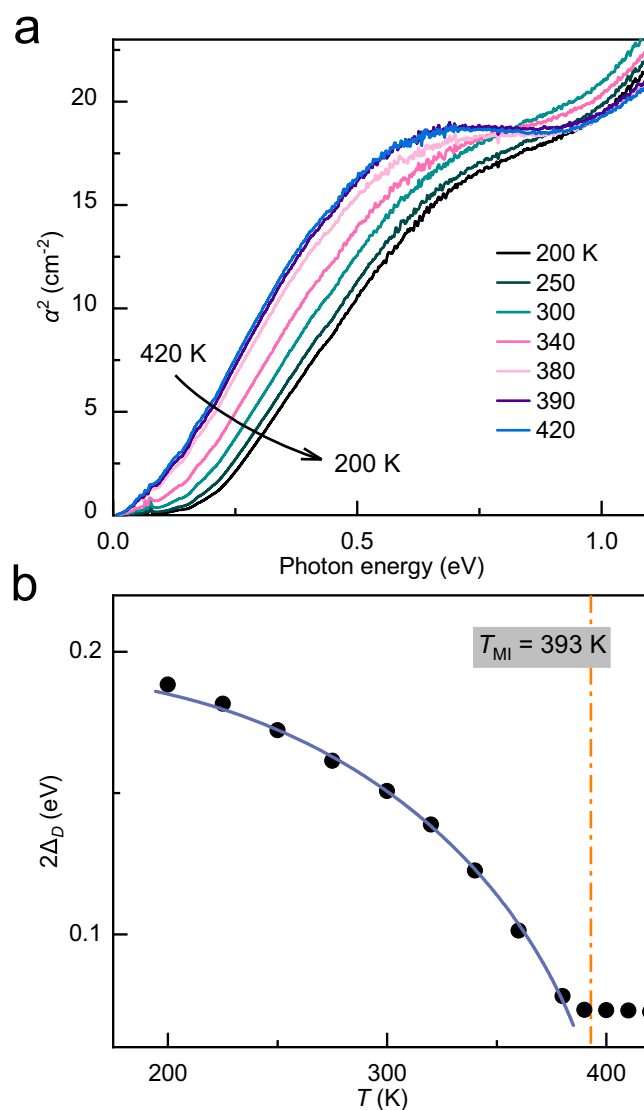


**Fig. 5 | Temperature-dependent infrared spectral analysis for CCNOO.** **a** Square of the absorption coefficient at various temperatures. **b** Temperature-dependent optical direct gap (filled circles) along with the BCS fitting (solid line). The vertical dot line indicates the phase transition temperature.

effects are included, FiM GGA + SOC calculations completely open an energy gap (Supplementary Fig. S11a), albeit with a small value of approximately 0.5 meV. Therefore, from the perspective of electronic band evolution, spin fluctuations and SOC effects can induce upward (downward) shifts of electron (hole) bands. Furthermore, when  $U$  is considered (refer to Supplementary Figs. S12 and S11b), the local Coulomb repulsion pushes the occupied  $d$  orbitals to a lower energy level and the unoccupied states to a higher one, resulting in the opening of a larger band gap up to 0.23 eV in FiM GGA + SOC +  $U$  calculations. Consequently, an electronic correlation and SOC effects-assisted high-temperature FiM spontaneous magnetization triggered MIT is rarely realized in the current CCNOO via Lifshitz's scenario.

## Discussion

In summary, we successfully synthesized a novel  $3d/5d$  hybridized A- and B-site ordered quadruple perovskite oxide  $\text{CaCu}_3\text{Ni}_2\text{Os}_2\text{O}_{12}$  at high-pressure (8 GPa) and high-temperature (1423 K) conditions. This material exhibits robust spontaneous magnetization below  $T_C = 393$  K, showing a saturated magnetic moment of  $2.15 \mu_B/\text{f.u.}$  at 300 K, which increases to  $3.36 \mu_B/\text{f.u.}$  at 2 K. Three kinds of magnetic ions

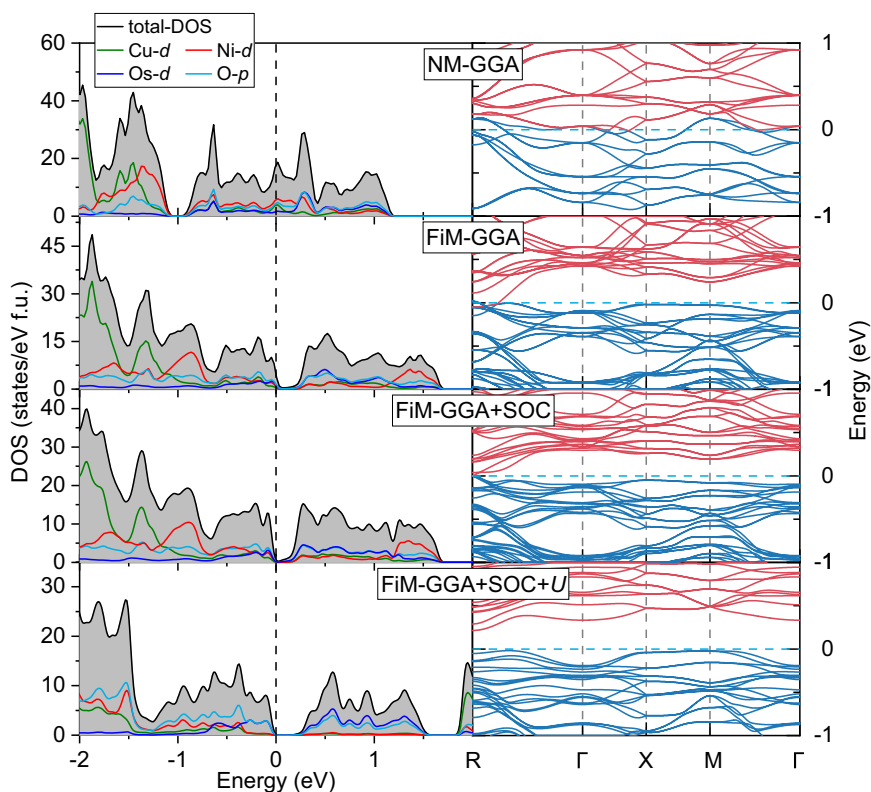


**Fig. 6 | Evolution of electronic band structures of CCNOO.** The partial DOS (left) and the band structure (right) considering spin order, SOC, and  $U$ .

form a long-range FiM ground state with the spin coupling of  $\text{Cu}^{2+}(\uparrow)\text{-Ni}^{2+}(\uparrow)\text{-Os}^{6+}(\downarrow)$ . Moreover, a joint MIT occurs during the FiM transition at  $T_C$  ( $T_{\text{MI}}$ ). Infrared optical spectroscopy further reveals the presence of a direct bandgap at the onset of  $T_C$ . Theoretical calculations indicate that the FiM spin order significantly renormalizes the electronic band structure, and electronic correlation and SOC effects can further open the energy bandgap, leading to the occurrence of the MIT. The simultaneous high-temperature magnetic and electrical transitions accompanied by the substantial spontaneous magnetization make the current CCNOO quite unique among all reported MIT materials, highlighting the promising potentials for advanced multifunctional electronic and spintronic applications.

## Methods

### Material synthesis

Highly pure (>99.9%) powders of CaO, CuO, NiO, Os, and  $\text{KClO}_4$  were used as starting materials and thoroughly mixed in an argon-filled glove box. The mixture was then sealed into a platinum capsule and subjected to high-pressure and high-temperature treatment at 8 GPa and 1423 K for 60 min on a cubic-anvil-type apparatus. The resulting polycrystalline pellet was rinsed with deionized water to eliminate the residual KCl. Finally, the single-phase powders were sintered at 8 GPa and 1273 K for 10 min, yielding the bulk sample that was subsequently used for physical property measurements.

### X-ray and neutron diffraction

SXRD was performed using a large Debye-Scherrer camera installed at the BL02B2 beamline ( $\lambda = 0.42014 \text{ \AA}$ ) of SPring-8, Japan. Temperature-dependent laboratory XRD measurements were conducted on a Rigaku-SmartLab diffractometer with  $\text{Cu } K_\alpha$  radiation. The SXRD and XRD patterns were analyzed using the Rietveld refinement method implemented in the GSAS program<sup>35</sup>. Temperature-dependent NPD was performed using the Peking University High Intensity Powder Diffractometer (PKU-HIPD) at China Institute of Atomic Energy (CIAE).

The powder samples were loaded in a cylindrical vanadium sample holder, and a Si (115) monochromator was used to produce a monochromatic neutron beam ( $\lambda = 1.478 \text{ \AA}$ ). The NPD patterns were analyzed using the Rietveld package, FullProf suite<sup>36</sup>.

### XAS and XMCD measurements

The soft XAS at the Cu- and Fe- $L_{2,3}$  edges were measured with the total electron yield mode at TLS BL11A beamline of synchrotron NSRRC, Taiwan. The hard XAS at the Os- $L_{2,3}$  edges was measured with transmission geometry at the TPS BL44A beamline of NSRRC. XMCD measurements at the Cu- and Ni- $L_{2,3}$  edges were collected under 6 T and 10 K at the DEIMOS beamline of SOLEIL synchrotron, France. The Os- $L_3$  edge was collected under 1.2 T and 10 K at the ODE beamline of SOLEIL.

### Magnetic, electrical, and thermal measurements

The magnetic susceptibility and magnetization were measured on a superconducting quantum interference device magnetometer (Quantum Design, MPMS-VSM). Both zero-field-cooling (ZFC) and field-cooling (FC) modes were used to measure the magnetic susceptibility between 2 and 300 K at 0.1 T. The magnetic data above 300 K were collected on a MicroSense vibrating sample magnetometer. The isothermal magnetization was measured at 2 K, 200 K, 300 K, and 400 K in a magnetic field range of  $-5 \text{ T}$  and  $+5 \text{ T}$ . The measurements of resistivity between 2 K and 400 K were conducted on a physical property measurement system (Quantum Design, PPMS-9T). Resistivity between 400 K and 650 K was measured on a homemade electrical measurement system. The standard four-probe method was adopted in resistivity measurements. The thermogravimetry (TG) and differential thermal analysis (DTA) were measured on a Labsys Evo STA TG/DTA system under  $\text{N}_2$  atmosphere. The sample was placed in a corundum crucible, heated up to 1300 K with a rate of 10 K/min, held for 10 min, and then cooled to RT with the same rate. The differential scanning calorimetry (DSC) was measured under an Ar atmosphere. The sample was placed in an aluminum

crucible, heated up to 500 K with a rate of 5 K/min, held for 5 min, and then cooled to RT with the same rate.

### Infrared spectroscopy measurements

A well-polished bulk disc specimen of CCNOO with 3 mm diameter was used to measure temperature-dependent infrared reflectivity spectra  $R(\omega)$  from 200 K to 420 K within 0.0075–1.5 eV, using a Bruker 80 v Fourier transform infrared spectrometer with a commercial ARS-Helitrans cryostat. An in-situ gold evaporation technique has been used for obtaining the absolute reflectivity of the sample. The reflectivity within the visible-UV range (1.25–5 eV) was measured at RT with an Avaspec 2048 × 14 optical fiber spectrometer. Then, Kramers–Kronig analysis of  $R(\omega)$  was applied to obtain the optical conductivity spectra. For low-frequency extrapolation, a constant reflectivity was used. Above the highest-measured frequency,  $R(\omega)$  was assumed to be constant up to 10 eV, above which a free-electron response ( $R(\omega) \propto \omega^4$ ) was used.

### Theoretical calculations

First-principles numerical calculations were performed using the WIEN2K code<sup>37</sup>, which implemented the full-potential linearized augmented plane-wave method. The crystal structural parameters adopted for the numerical calculations were derived from the SXRD refinement at 300 K. The muffin-tin radii were 2.48 a.u. for Ca, 1.96 a.u. for Cu, 2.05 a.u. for Ni, 1.98 a.u. for Os, and 1.62 a.u. for O. The maximum modulus for the reciprocal vectors  $K_{\max}$  was chosen as  $R_{\text{MT}} \times K_{\max} = 8.0$ . We took the generalized-gradient approximation Perdew–Burke–Ernzerhof (GGA-PBE)<sup>38</sup> exchange-correlation energy and used 1000  $k$ -point meshes for the whole Brillouin zone. In our GGA +  $U$  calculations, we assigned an effective  $U$  value of 5 eV for Cu, 4 eV for Ni, and 2 eV for Os, while  $J$  was set to 0.8 eV. These parameter values were determined through experimental spectral analysis<sup>39</sup> and theoretical efforts aimed at obtaining physically meaningful results<sup>14,40,41</sup>. In order to calculate the magnetic ground state, we proposed four different magnetic structures as shown in Fig. S6 and Table S4 [i.e., FM Cu<sup>2+</sup>(↑)Ni<sup>2+</sup>(↑)Os<sup>6+</sup>(↑); FiM1: Cu<sup>2+</sup>(↑)Ni<sup>2+</sup>(↑)Os<sup>6+</sup>(↓); FiM2: Cu<sup>2+</sup>(↓)Ni<sup>2+</sup>(↑)Os<sup>6+</sup>(↑); FiM3: Cu<sup>2+</sup>(↓)Ni<sup>2+</sup>(↑)Os<sup>6+</sup>(↓)]. The nearest-neighbor effective exchange couplings between magnetic ions were calculated using the energy differences of the four magnetic structures:

$$E(\text{FiM1}) = E_0 + 12J_{\text{Cu-Ni}}S_{\text{Cu}}S_{\text{Ni}} - 12J_{\text{Ni-Os}}S_{\text{Ni}}S_{\text{Os}} - 12J_{\text{Cu-Os}}S_{\text{Cu}}S_{\text{Os}}, \quad (1)$$

$$E(\text{FiM2}) = E_0 - 12J_{\text{Cu-Ni}}S_{\text{Cu}}S_{\text{Ni}} + 12J_{\text{Ni-Os}}S_{\text{Ni}}S_{\text{Os}} - 12J_{\text{Cu-Os}}S_{\text{Cu}}S_{\text{Os}}, \quad (2)$$

$$E(\text{FiM3}) = E_0 - 12J_{\text{Cu-Ni}}S_{\text{Cu}}S_{\text{Ni}} - 12J_{\text{Ni-Os}}S_{\text{Ni}}S_{\text{Os}} + 12J_{\text{Cu-Os}}S_{\text{Cu}}S_{\text{Os}}, \quad (3)$$

$$E(\text{FM}) = E_0 + 12J_{\text{Cu-Ni}}S_{\text{Cu}}S_{\text{Ni}} + 12J_{\text{Ni-Os}}S_{\text{Ni}}S_{\text{Os}} + 12J_{\text{Cu-Os}}S_{\text{Cu}}S_{\text{Os}}. \quad (4)$$

### Data availability

All raw data generated in this study are provided in the Source Data file. Source data are provided with this paper.

### References

- Imada, M., Fujimori, A. & Tokura, Y. Metal-insulator transitions. *Rev. Mod. Phys.* **70**, 1039–1263 (1998).
- Tokura, Y. & Tomioka, Y. Colossal magnetoresistive manganites. *J. Magn. Magn. Mater.* **200**, 1–23 (1999).
- Coey, J. M. D., Viret, M. & von Molnár, S. Mixed-valence manganites. *Adv. Phys.* **48**, 167–293 (1999).
- Von Helmolt, R., Wecker, J., Holzapfel, B., Schultz, L. & Samwer, K. Giant negative magnetoresistance in perovskitelike  $\text{La}_{2/3}\text{Ba}_{1/3}\text{MnO}_x$  ferromagnetic films. *Phys. Rev. Lett.* **71**, 2331–2333 (1993).
- Jin, S. et al. Thousandfold change in resistivity in magnetoresistive La–Ca–Mn–O films. *Science* **264**, 413–415 (1994).
- Khan, M. A., Sun, J., Li, B., Przybysz, A. & Kosel, J. Magnetic sensors—a review and recent technologies. *Eng. Res. Express* **3**, 022005 (2021).
- Wesenberg, D., Liu, T., Balzar, D., Wu, M. & Zink, B. L. Long-distance spin transport in a disordered magnetic insulator. *Nat. Phys.* **13**, 987–993 (2017).
- Yang, Z., Ko, C. & Ramanathan, S. Oxide electronics utilizing ultrafast metal-insulator transitions. *Annu. Rev. Mater. Res.* **41**, 337–367 (2011).
- Mott, N. F. The basis of the electron theory of metals, with special reference to the transition metals. *Proc. Phys. Soc. Lond. Sect. A* **62**, 416–422 (1949).
- Hubbard, J. & Flowers, B. H. Electron correlations in narrow energy bands. *Proc. R. Soc. Lond. A. Math. Phys. Sci.* **276**, 238–257 (1997).
- Slater, J. C. Magnetic effects and the Hartree–Fock Equation. *Phys. Rev.* **82**, 538–541 (1951).
- Shi, Y. G. et al. Continuous metal-insulator transition of the anti-ferromagnetic perovskite  $\text{NaOsO}_3$ . *Phys. Rev. B* **80**, 161104 (2009).
- Hiroi, Z., Yamaura, J., Hirose, T., Nagashima, I. & Okamoto, Y. Lifshitz metal-insulator transition induced by the all-in/all-out magnetic order in the pyrochlore oxide  $\text{Cd}_2\text{Os}_2\text{O}_7$ . *APL Mater.* **3**, 041501 (2015).
- Kim, B. et al. Lifshitz transition driven by spin fluctuations and spin-orbit renormalization in  $\text{NaOsO}_3$ . *Phys. Rev. B* **94**, 241113 (2016).
- Lifshitz, M. Anomalies of electron characteristics of a metal in the high pressure region. *Sov. Phys. JETP* **11**, 1130–1135 (1960).
- Feng, H. L. et al.  $\text{Ba}_2\text{NiOsO}_6$ : a Dirac–Mott insulator with ferromagnetism near 100 K. *Phys. Rev. B* **94**, 235158 (2016).
- Feng, H. L., Schnelle, W., Tjeng, L. H. & Jansen, M. Synthesis, crystal structures, and magnetic properties of double perovskites  $\text{SrLaNiOsO}_6$  and  $\text{BaLaNiOsO}_6$ . *Solid State Commun.* **243**, 49–54 (2016).
- Morrow, R. et al. Magnetism in  $\text{Ca}_2\text{CoOsO}_6$  and  $\text{Ca}_2\text{NiOsO}_6$ : unraveling the mystery of superexchange interactions between 3d and 5d ions. *Chem. Mater.* **28**, 3666–3675 (2016).
- Ye, X. et al. A–B intersite cooperation-enhanced water splitting in quadruple perovskite oxide  $\text{CaCu}_3\text{Ir}_4\text{O}_{12}$ . *Chem. Mater.* **33**, 9295–9305 (2021).
- Tjeng, L. H., Chen, C. T. & Cheong, S.-W. Comparative soft-x-ray resonant-photoemission study on  $\text{Bi}_2\text{Sr}_2\text{CaCu}_2\text{O}_8$ ,  $\text{CuO}$ , and  $\text{Cu}_2\text{O}$ . *Phys. Rev. B* **45**, 8205–8208 (1992).
- Guo, H. et al. Antiferromagnetic correlations in the metallic strongly correlated transition metal oxide  $\text{LaNiO}_3$ . *Nat. Commun.* **9**, 43 (2018).
- Chen, J. et al. Enhanced magnetization of the highest- $T_C$  ferrimagnetic oxide  $\text{Sr}_2\text{CrOsO}_6$ . *Phys. Rev. B* **102**, 184418 (2020).
- Smart, J. S. The Néel theory of ferrimagnetism. *Am. J. Phys.* **23**, 356–370 (1955).
- Liu, Z. et al. Observation of A-site antiferromagnetic and B-site ferrimagnetic orderings in the quadruple perovskite oxide  $\text{CaCu}_3\text{Co}_2\text{Re}_2\text{O}_{12}$ . *Phys. Rev. B* **103**, 014414 (2021).
- Feng, H. L. et al. From antiferromagnetism to high- $T_C$  weak ferromagnetism manipulated by atomic rearrangement in  $\text{Ba}_3\text{NiOs}_2\text{O}_9$ . *Phys. Rev. Mater.* **4**, 064420 (2020).
- Wang, X. et al. Comparative study on the magnetic and transport properties of B-site ordered and disordered  $\text{CaCu}_3\text{Fe}_2\text{Os}_2\text{O}_{12}$ . *Inorg. Chem.* **61**, 16929–16935 (2022).

27. Thole, B. T., Carra, P., Sette, F. & van der Laan, G. X-ray circular dichroism as a probe of orbital magnetization. *Phys. Rev. Lett.* **68**, 1943–1946 (1992).
  28. Carra, P., Thole, B. T., Altarelli, M. & Wang, X. X-ray circular dichroism and local magnetic fields. *Phys. Rev. Lett.* **70**, 694–697 (1993).
  29. Fernandez, V., Vettier, C., de Bergevin, F., Giles, C. & Neubeck, W. Observation of orbital moment in NiO. *Phys. Rev. B* **57**, 7870–7876 (1998).
  30. van der Laan, G. et al. Orbital polarization in NiFe<sub>2</sub>O<sub>4</sub> measured by Ni-2p x-ray magnetic circular dichroism. *Phys. Rev. B* **59**, 4314–4321 (1999).
  31. Shklovskii, B. I. & Efros, A. L. *Electronic Properties of Doped Semiconductors*. 45 (Springer Berlin Heidelberg, Berlin, 1984).
  32. Sohn, C. H. et al. Optical spectroscopic studies of the metal-insulator transition driven by all-in–all-out magnetic ordering in 5d pyrochlore Cd<sub>2</sub>Os<sub>2</sub>O<sub>7</sub>. *Phys. Rev. Lett.* **115**, 266402 (2015).
  33. Padilla, W. J., Mandrus, D. & Basov, D. N. Searching for the Slater transition in the pyrochlore Cd<sub>2</sub>Os<sub>2</sub>O<sub>7</sub> with infrared spectroscopy. *Phys. Rev. B* **66**, 035120 (2002).
  34. Cheng, J.-G. et al. Possible Kondo physics near a metal-insulator crossover in the A-site ordered perovskite CaCu<sub>3</sub>Ir<sub>4</sub>O<sub>12</sub>. *Phys. Rev. Lett.* **111**, 176403 (2013).
  35. Larson, A. C. & Dreele, R. B. V. General structure analysis system (GSAS). *Alamos Natl. Lab. Rep. LAUR* **86**, 784 (2004).
  36. Rodríguez-Carvajal, J. Recent advances in magnetic structure determination by neutron powder diffraction. *Phys. B* **192**, 55–69 (1993).
  37. Blaha, P., Schwarz, K., Madsen, G., Kvasnicka, D. & Luitz, J. *WIEN2k: An Augmented Plane Wave plus Local Orbitals Program for Calculating Crystal Properties* (Technische Universität Wien, Vienna, 2001).
  38. Perdew, J. P., Burke, K. & Ernzerhof, M. Generalized gradient approximation made simple. *Phys. Rev. Lett.* **77**, 3865–3868 (1996).
  39. Anisimov, V. I., Solov'ev, I. V., Korotin, M. A., Czyżyk, M. T. & Sawatzky, G. A. Density-functional theory and NiO photoemission spectra. *Phys. Rev. B* **48**, 16929–16934 (1993).
  40. Shinaoka, H., Miyake, T. & Ishibashi, S. Noncollinear magnetism and spin-orbit coupling in 5d pyrochlore oxide Cd<sub>2</sub>Os<sub>2</sub>O<sub>7</sub>. *Phys. Rev. Lett.* **108**, 247204 (2012).
  41. Li, H., Zhu, Z., Ge, Z., Sun, A. & Tian, Y. Ferrimagnetic semiconductor with a direct bandgap. *Appl. Phys. Lett.* **116**, 122401 (2020).
- Radiation Research Institute (2023B1575 and 2024A1506). The authors acknowledge the support from the Max Planck-POSTECH-Hsinchu Center for Complex Phase Materials.

## Author contributions

Y.L. conceived and supervised the study. X.Y. and Y.Y. prepared the sample and performed analyses of the crystal structure and physical properties. Y.C., M.L., Q.W., and Y.-f.Y. conducted theoretical calculations. Z.L. and X.Q. measured the infrared spectroscopy. X.W., Z.H., H.L., C.T.C., and C.P. conducted XAS. Z.P. conducted SXR. P.O., L.N., and F.B. conducted XMCD. W.Y. and J.Y. performed low-temperature NPD. J.C., P.Y., and T.X. provided insights and interpretation of the results. X.Y. and Y.L. wrote the manuscript. All authors reviewed the results and provided feedback on the paper.

## Competing interests

The authors declare no competing interests.

## Additional information

**Supplementary information** The online version contains supplementary material available at <https://doi.org/10.1038/s41467-025-59041-5>.

**Correspondence** and requests for materials should be addressed to Yi-feng Yang or Youwen Long.

**Peer review information** *Nature Communications* thanks the anonymous reviewers for their contribution to the peer review of this work. A peer review file is available.

**Reprints and permissions information** is available at <http://www.nature.com/reprints>

**Publisher's note** Springer Nature remains neutral with regard to jurisdictional claims in published maps and institutional affiliations.

**Open Access** This article is licensed under a Creative Commons Attribution-NonCommercial-NoDerivatives 4.0 International License, which permits any non-commercial use, sharing, distribution and reproduction in any medium or format, as long as you give appropriate credit to the original author(s) and the source, provide a link to the Creative Commons licence, and indicate if you modified the licensed material. You do not have permission under this licence to share adapted material derived from this article or parts of it. The images or other third party material in this article are included in the article's Creative Commons licence, unless indicated otherwise in a credit line to the material. If material is not included in the article's Creative Commons licence and your intended use is not permitted by statutory regulation or exceeds the permitted use, you will need to obtain permission directly from the copyright holder. To view a copy of this licence, visit <http://creativecommons.org/licenses/by-nc-nd/4.0/>.

© The Author(s) 2025

## Acknowledgements

The authors thank G. Chen, H. M. Weng, and J. P. Hu for fruitful discussions. This work was financially supported by the National Key R&D Program of China (grant no. 2021YFA1400300 (Y.L.)), the National Natural Science Foundation of China (grant no. 12425403 (Y.L.), 12261131499 (Y.L.), 11934017 (Y.L.), 11974397 (Y.L.), 12304268 (X.Y.), and 12304159 (X.W.)), the China Postdoctoral Science Foundation (grant no. 2023M743741 (X.Y.)), and the Chinese Academy of Sciences (grant no. XDB33000000 (Y.L. and J.C.)). The research in Dresden was partially supported by the DFG through SFB 1143. The SXR experiments were performed at SPring-8 with the approval of the Japan Synchrotron